Detection of antibodies against SARS-CoV-2 spike protein by gold nanospikes in an opto-microfluidic chip

Riccardo Funari[a,*], Kang-Yu Chu[a] and Amy Q Shen[a,*]

[a]*Micro/Bio/Nanofluidics Unit, Okinawa Institute of Science and Technology Graduate University, 1919-1 Tancha, Onna-son, Okinawa, 904-0495 Japan*

ARTICLE INFO

Keywords:
SARS-CoV-2
COVID-19
Antibody
LSPR
Microfluidics
Gold electrodeposition

ABSTRACT

The ongoing global pandemic of severe acute respiratory syndrome coronavirus 2 (SARS-CoV-2) has led to active research in its associated diagnostics and medical treatments. While quantitative reverse transcription polymerase chain reaction (qRT–PCR) is the most reliable method to detect viral genes of SARS-CoV-2, serological tests for specific antiviral antibodies are also important as they identify false negative qRT–PCR responses, track how effectively the patient's immune system is fighting the infection, and are potentially helpful for plasma transfusion therapies. In this work, based on the principle of localized surface plasmon resonance (LSPR), we develop an opto-microfluidic sensing platform with gold nanospikes, fabricated by electrodeposition, to detect the presence and amount of antibodies specific to the SARS-CoV-2 spike protein in 1 μL of human plasma diluted in 1 mL of buffer solution, within $\sim$ 30 min. The target antibody concentration can be correlated with the LSPR wavelength peak shift of gold nanospikes caused by the local refractive index change due to the antigen-antibody binding. This label-free microfluidic platform achieves a limit of detection of $\sim$ 0.08 ng/mL ($\sim$ 0.5 pM), falling under the clinical relevant concentration range. We demonstrate that our opto-microfluidic platform offers a promising point-of-care testing tool to complement standard serological assays and make SARS-CoV-2 quantitative diagnostics easier, cheaper, and faster.

1. Introduction

The recent worldwide outbreak of severe acute respiratory syndrome related coronavirus 2 (SARS-CoV-2) (Wu et al., 2020) has led to unprecedented pressure on national healthcare systems (Fauci et al., 2020). The World Health Organization (WHO) advised the international community to perform extensive diagnostic tests to reduce the spreading of the virus and decrease the number of unreported cases (i.e., asymptomatic or mild cases) (Li et al., 2020; Zhao et al., 2020). This strongly motivates the researchers to develop reliable testing tools to make SARS-CoV-2 diagnostics easier, cheaper and more accessible (Dincer et al., 2019; Choi, 2020; Morales-Narváez and Dincer, 2020; Zhu et al., 2020; Santiago, 2020; Seo et al., 2020; Bhalla et al., 2020). While quantitative reverse transcription polymerase chain reaction (qRT–PCR) is the most reliable method to detect the genome of SARS-CoV-2 at the early stage of the infection (Corman et al., 2020; Chu et al., 2020; Moitra et al., 2020), serological tests for viral antibodies are equally important as they can identify false negative qRT–PCR responses because the virus concentration tends to become low at the late stage of the infection (La Marca et al., 2020). In addition, sampling for antibodies are easier because antibodies are more stable than RNAs. Even though it takes several days to develop sufficient amount of antibody in blood plasma or serum once a patient is infected by SARS-CoV-2, serological analysis is crucial for the identification of asymptomatic infections to further control the spread of the virus (Paiva et al., 2020; Du et al., 2020; Cui and Zhou, 2020; Day, 2020). Finally, the antibody tests can help to track how effectively the patient's immune system is fighting the infection and are potentially helpful for plasma transfusion therapies (Krammer and Simon, 2020; Winter and Hegde, 2020; Long et al., 2020; Roback and Guarner, 2020; Duan et al., 2020; Amanat et al., 2020; La Marca et al., 2020; Lee et al., 2020).

Several serological tests have received the Emergency Use Authorization (EUA) from the U.S. Food and Drug Administration (FDA) (U.S. Food and Drug Administration, 2020). Among them, enzyme linked immunosorbent assays (ELISA), chemiluminescent immunoassays, and neutralization assays (Muruato et al., 2020) are reliable but necessitate of trained operators and require hours or even days to perform the analysis (John Hopkins Center for Health

*Corresponding authors
riccardo.funari@oist.jp (R. Funari); amy.shen@oist.jp (A.Q. Shen)
https://groups.oist.jp/mbnu (A.Q. Shen)
ORCID(s): 0000-0003-1786-3833 (R. Funari); 0000-0002-1222-6264 (A.Q. Shen)

Security, 2020). On the other hand, rapid diagnostic tests such as lateral flow assays, are easier to use and provide the results quickly (i.e, 10–30 min), but they offer only qualitative information and their accuracy is not always sufficient (Carter et al., 2020; Udugama et al., 2020; John Hopkins Center for Health Security, 2020). A comprehensive survey of the existing serological tests published by FDA is summarized in Table S1 in the Supplementary Material.

More recently, new diagnostic sensors (Xu et al., 2020) have been developed to support the standard SARS-CoV-2 diagnostic techniques by detecting the viral RNA by using CRISPR (clustered regularly interspaced short palindromic repeats) based assays (Huang et al., 2020) and plasmonics (Qiu et al., 2020), the viral surface proteins by field-effect transistors (Seo et al., 2020), membrane-engineered mammalian cells (Mavrikou et al., 2020), and toroidal plasmonic devices (Ahmadivand et al., 2020). In addition, new lateral flow assays based on immunochromatographic strips have also been established to identify the antibodies produced in blood in response to the viral infection with qualitative outputs (i.e., positive or negative) (Zeng et al., 2020).

Motivated by finding a reliable, rapid, and cost-effective alternative to existing serological methodologies for antibody detection (Dincer et al., 2019), we develop an opto-microfluidic biosensor platform to quantify the concentration of anti-SARS-CoV-2 spike protein antibodies in diluted human plasma by correlating the wavelength shift of the localized surface plasmon resonance (LSPR) peak of gold nanostructures in the microfluidic device upon binding interactions with the SARS-CoV-2 spike protein. The LSPR detection principle is based on the local refractive index changes around the metal nanostructures due to the biomolecule binding events (i.e., antigen-antibody binding). This leads to a red shift of the LSPR peak of the metal nanostructures, which is directly proportional to the target antibody concentration (Willets and Van Duyne, 2007; Mayer and Hafner, 2011). Another advantage of LSPR-based sensing is that the short decay length of the electromagnetic field in localized surface plasmons greatly reduces interfering effects from the bulk solution, which is desirable when analyzing complex samples such as blood plasma or serum containing fibrinogen, globulins, etc. (Szunerits and Boukherroub, 2012). Our optofluidic platform consists of a gold nanospike covered glass substrate, fabricated by gold electrodeposition (ED), integrated in a microfluidic chip coupled with a reflection probe to detect the presence of antibodies against the SARS-CoV-2 spike protein within $\sim$ 30 min in a diluted human plasma (1:1000), with the limit of detection (LOD) of $\sim$ 0.08 ng/mL ($\sim$ 0.5 pM), which falls under the clinical relevant concentration range (ng/mL–μg/mL in diluted plasma samples) (Brown et al., 2018; Humphrey and Batty, 1974; Long et al., 2020). Our work successfully demonstrates, for the first time, an opto-microfluidic chip to detect antibodies specific to the SARS-CoV-2 spike protein in real human plasma with high sensitivity and selectivity, without labeling agents, which can be expanded as a potential point-of-care antibody testing platform for real sample analysis.

2. Materials and Methods

2.1. Chemicals and Biological Materials

Glycerol, acetone, isopropanol (Sigma Aldrich, Japan) and MilliQ® water (Millipore, Japan) are used for the sensitivity measurements and sample preparation. Gold (III) chloride trihydrate (520918), human plasma (c), lead (II) acetate trihydrate (316512), goat anti-mouse IgG (M8642), mouse IgG (I5381), bovine serum albumin (BSA, A2153), and phosphate buffered saline (PBS) tablets (P4417) are purchased from Sigma Aldrich, Japan. Human C-Reactive Protein (CRP, 1707-CR-200) is obtained from R&D Systems, Japan. SARS-CoV-2 Spike Protein peptide (ABIN1382273) and anti-SARS-CoV-2 spike protein antibody (ABIN1030641) are purchased from antibodies-online.com, Germany. Interleukin 6 (IL-6, PHC0066) is purchased from Thermo Scientific, Japan. N-hydroxysuccinimide (NHS, 24500) and 1-ethyl-3-(3-dimethylaminopropyl)carbodiimide hydrochloride (EDC, 22980) are purchased from Thermo Scientific, Japan. 11-mercaptoundecanoic acid (450561) and 6-mercapto-1-hexanol (725226) are purchased from Sigma Aldrich, Japan. Polydimethylsiloxane (PDMS) is purchased from Dow Corning, Japan.

2.2. Gold Electrodeposition

Gold (Au) coated glass slides (CA134, 50 Å of chromium as adhesion layer and 1,000 Å of Au) are purchased from Dynasil's EMF, USA. The glass slides are cut in 25 mm $\times$ 25 mm pieces using an automatic dicing saw (DAD322, Disco, Japan) and cleaned sequentially at room temperature via sonication for 5 min in acetone (ACE), isopropanol (IPA) and MilliQ® and dried with a stream of nitrogen. The electrodeposition (ED) process is performed using an Ivium CompactStat.h (Ivium Technologies, Netherlands) in a bottom magnetic mount electrochemical cell (BMM EC 15 mL) from redox.me, Sweden. The gold coated glass slide is mounted at the bottom of the cell and used as the working electrode, while a Pt wire and a Ag/AgCl (3 M NaCl) electrode are used as the counter and reference electrode,

respectively. The electrolyte solution contains 8 mM of $AuCl_3$ and 0.5 mM of $Pb(CH_3COO)_2$ (Sabri et al., 2014), and its cyclic voltammetry profile is shown in the Supplementary Material (Fig. S1a).

The electrodeposition (ED) process offers great flexibility in manipulating nanostructure properties (e.g., size, shape, etc.) (Tian et al., 2006; Cherevko and Chung, 2011; Sabri et al., 2014, 2016; Lopa et al., 2019; Mohammadniaei et al., 2019) for a variety of biosensing applications (Stine, 2019), by adjusting the electrolyte concentration, the ED time, and the voltage applied to the electrode. In this work, a fixed voltage (-1.85 V) is applied to the gold coated glass slides, while deposition times are varied at 90, 180, 240, 300, 390, 480, 600 and 720 s respectively. Since the 480 s ED time produces the most uniform Au nanospikes with the best optical properties (see chronoamperometric profiles of different ED conditions in Supplementary Material (Fig. S1b)), this ED condition will be used for all the experiments. Finally, the Au nanospike (with an area of ≈ 1 cm^2) covered glass substrates are washed 3 times with MilliQ® water and dried with a gentle stream of nitrogen before surface functionalization steps.

2.3. Morphological Characterization of Gold Nanospikes by Scanning Electron Microscopy

The scanning electron microscopy (SEM) is carried out by using a high performance scanning electron microscope (FEI Quanta 250 FEG, Thermo Fisher Scientific). Images are acquired at 20 kV, with a magnification of 30,000 × and 100,000 × inside a vacuum chamber maintained at a pressure of 10^{-4} Pa. The top view of the Au nanospike covered substrate is captured with the electron gun placed normal to the substrate, while the side view of the substrate is captured by tilting the substrate at 40°.

2.4. Functionalization of Gold Nanospikes

A 1:1 mixture of 1 mM of MUA (11-mercaptoundecanoic acid) and 9 mM of MCH (6-mercaptohexanol) in pure ethanol (99.9 %) is prepared in the fume hood. The Au nanospike covered substrate is placed in a glass Petri dish and exposed to the thiol mixture in a cold room at 4°C for 14–16 h. To prevent the evaporation of the ethanol, the glass Petri dish is kept in a humid chamber during the functionalization step. After incubation, the solution inside the wells is rinsed with 1 mM MCH. The substrate is then incubated for 1 h with a 1 mM solution of MCH to backfill the gold surface, at room temperature in the fume hood. Next, the MCH solution is rinsed with ethanol. To activate the surface, the Au nanospikes are incubated with a 1:1 solution of 10 mM NHS (N-Hydroxysuccinimide) and 40 mM of EDC (1-Ethyl-3-(3-dimethytaminopropyl) carbodiimide) in MilliQ water at room temperature for 15 min. The Au nanospikes are next exposed to an antigen sample (either 1 μg/mL murine IgG or 1 μg/mL SARS-CoV-2 S peptide in PBS) for 2 h at 4°C. The Au nanospike covered substrate is then washed with PBS and incubated with a 100 μg/mL solution of BSA for 30 min at room temperature to block the remaining free surface and prevent non-specific interactions. This functionalization procedure is verified by recording the LSPR spectra in air after each step of the protocol (i.e., The LSPR peak positions at each stage of the functionalization protocol are reported in Fig. S5 in the Supplementary Material). The detailed description of the LSPR measurements and the acquisition conditions (i.e., probe position, light intensity, acquisition time) are reported in the next subsection.

2.5. Opto-microfluidic Platform Assembly

The functionalized Au nanospike covered substrate (I in Fig. 1a) is next bonded to a polydimethylsiloxane (PDMS) slab (III in Fig. 1a) by a 85 μm thick double-coated adhesive polyester tape (5302A from Nitto, Japan), II in Fig. 1a. The polyester tape is cut by a CO_2 laser cutter (VLS3.5 from Universal Laser Systems, Inc., USA) in 1.8 cm × 1.8 cm squares. The laser cutter is also used to remove a 1.2 cm × 0.2 cm area from the middle of the tape, which serves as the microfluidic channel. The PDMS slab (III in Fig. 1a) is 2 cm × 2 cm × 3 mm (length × width × height). Holes of 1 mm and 1.5 mm in diameter are punched in the PDMS slab by using disposable biopsy punchers (Kai Medical, Japan). The outer holes are used for sample delivery (sample volume of 1 mL), facilitated by a plastic syringe via a syringe pump at a flow rate of 30 μL/min, with Intramedic polyethylene tubes (427406, BD, Japan). The center hole is used to house the optical probe as shown in Fig. 1b.

The optical setup consists of a homemade reflective fiber-optic probe, light source (a white light tungsten halogen lamp (HL-2000-HP-FHSA, Ocean Insight, Inc., Germany)) and a detector (a UV-Vis spectrometer, USB-4000-ES from Ocean Insight, Inc., Germany). As shown in Fig. 1a and b, two 600 μm optical fibers (FP600ERT, Thorlabs) are used to excite the Au nanospikes and collect the reflected light. A stainless steel tube (ID 1.2 mm) is used to enclose the fibers in the reflection probe. The probe position is precisely regulated by a triaxial moving stage to keep the probe depth constant in the microfluidic chip for all experiments. After inserting the probe and the tubing in the PDMS slab, the holes are sealed with silicone glue to prevent leakages and air bubble formation (Fig. 1c). Note that the hardware

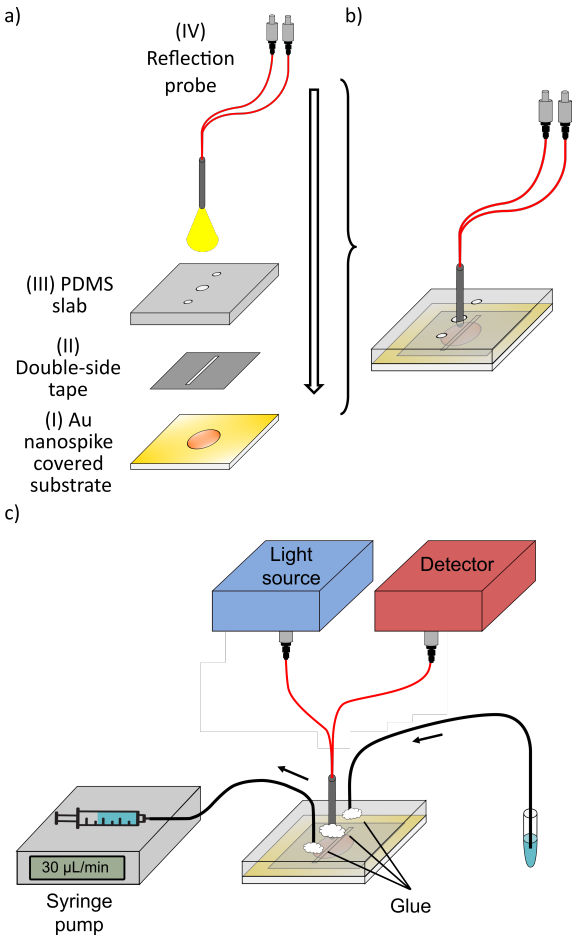

Figure 1: Opto-microfluidic design and experimental setup. Various components (from I to IV) shown in (a) are assembled into an integrated optofluidic device (b). The samples are delivered to the microfluidic platform by a syringe pump with polyethylene tubings (c). Silicone-based glue is used to seal the device. The reflective fiber optic probe delivers the light provided by the light source to excite the Au nanospikes embedded in the opto-microfluidic chip. The same probe collects the reflected light to the detector.

components of the setup (i.e., spectrometer, light source and fiber optics cost ≈ 8000 USD in total) are reusable. The material costs for a single opto-microfliudic chip is ≈ 2 USD, but the cost can be reduced by optimizing the fabrication procedure for the scale up production. Once the chip is assembled and the experiment is initiated, we use a MATLAB graphic user interface (GUI) to record and process the absorbance spectrum every 10 s.

3. Results and Discussion

3.1. Morphological and Optical Properties of Gold Nanospikes

The morphological characteristics of the Au nanospikes fabricated by different ED times (i.e., from 90 to 720 s) have been analyzed by SEM (Fig. S2). Among these conditions, samples prepared at 480 s ED time display the most regular and uniform Au nanospikes with a surface coverage of ≈ 20% (Fig. 2), with the strongest light absorption at ≈ 513 nm (see absorption spectrum in Fig. 3a). Thus, all the results shown below are based on this fabrication protocol.

The refractive index (RI) sensitivity of the pristine Au nanospikes in the opto-microfluidic device is calculated by measuring the wavelength shift in the LSPR peak position when solutions with different refractive indexes (RI) are delivered to the microfluidic chip. Specifically, water and glycerol mixtures with concentration ranging from 10 to 50% w/w are used to vary the refractive indexes. The spectra of the gold nanospikes exposed to these solutions are shown in Fig. 3b, while the LSPR peak shift versus the RI of the solution is plotted in Fig. 3c. The refractive index sensitivity of

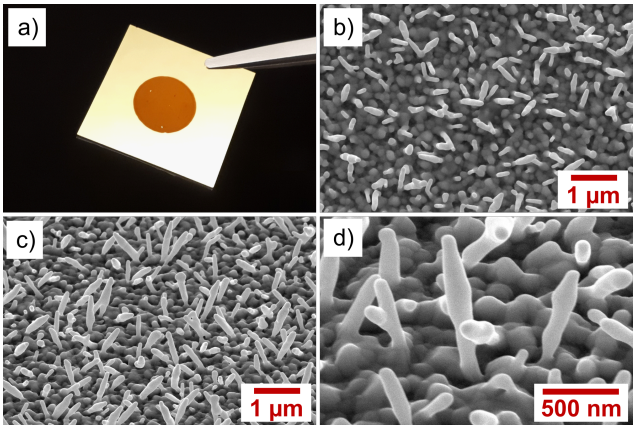

Figure 2: (a) Photo snapshot of the gold coated glass slide modified by electrodeposition. The reddish circular area represents the portion covered by the Au nanospikes. SEM images of Au nanospikes: (b) 30,000 ×, top view; (c) 30,000 ×, tilted (40°); and (d) 100,000 ×, tilted (40°).

the Au nanospike covered substrate is calculated to be 183 nm/RIU. This value is comparable with the refractive index sensitivity of gold nanostructures reported in literature (e.g., from 44 to 703 nm/RIU) (Chen et al., 2008). Even though gold nanospikes fabricated by ED in our work do not have the highest RI sensitivity, the nanofabrication procedure we have developed for Au nanospikes is extremely easy, cheap (no need for the clean room facility), and fast (480 s), thus suitable for scale up productions.

3.2. Anti-IgG Antibody Detection in PBS

Before employing our opto-microfluidic device in detecting antibodies against the SARS-CoV-2 Spike protein, we first use a model IgG/anti-IgG system to validate the accuracy and reliability of the platform. As described in Section 2.4, after fabricating the Au nanospike covered substrate, we coat the Au nanospikes with a self-assembled monolayer (SAM) of alkyl thiols. Next, we immobilize the antigen (i.e., murine IgG in this case) on the treated substrate, then block the remaining free surface with BSA to prevent nonspecific binding. Each step of the functionalization procedure is verified by measuring the LSPR peak shift in air (more details shown in Fig. S5a in the Supplementary Material). Subsequently, the functionalized Au nanospiked glass substrate is bonded with PDMS with a polyester tape, and coupled with the reflection probe.

Once the opto-microfluidic chip is assembled, PBS is delivered to the microfluidic channel by a syringe pump at a flow rate of 30 μL/min and the baseline from the PBS solution is recorded (see Fig. 4a where the LSPR peak position is monitored). After the sensor signal is stabilized in PBS, the PBS solution containing the antibody (1 ng/mL of anti-mouse IgG produced in goat) is injected to the microchannel. The change in the local refractive index due to the binding of the antibodies and the immobilized antigens on the Au nanospikes produces a robust red shift in the resonance peak position, which stabilizes in $\approx$ 15 min. Pure PBS is then injected to remove weakly bonded and nonspecific molecules. The LSPR spectra of functionalized gold nanospikes exposed to anti-IgG samples with concentrations ranging from 0.1 ng/mL to 10 μg/mL are shown in Fig. 4b. The wavelength shift measured after the washing step with PBS ($\approx$ 3 nm for 1 ng/mL antibody sample) is correlated with the concentration of specific antibodies in the test sample and is used to calibrate the sensor response (Fig. 4c), which can be expressed using a Hill-type equation, a widely used model (Kurganov et al., 2001; Weiss, 1997) describing antigen-antibody interaction:

$$\Delta\lambda(IgG) = \Delta\lambda_{max}\frac{[IgG]}{k + [IgG]}, \tag{1}$$

where $\Delta\lambda_{max}$ is the wavelength shift at saturating sensor response, while k corresponds to the antigen-antibody affinity constant. The best fit of the sensor responses gives the values of $\Delta\lambda_{max} = 6.8 \pm 0.2$ nm and $k = 1.2 \pm 0.3$ ng/mL. Since the flowing PBS inside the microfluidic chip causes fluctuations of $\approx$ 0.35 nm in the LSPR peak position, the LOD is defined by considering the concentration of antibody producing a wavelength shift that is 3 times this noise (S/N = 3) (Long and Winefordner, 1983), i.e., $\approx$ 1 nm, which corresponds to the antibody concentration of $\approx$ 0.2 ng/mL ($\approx$ 1.3 pM).

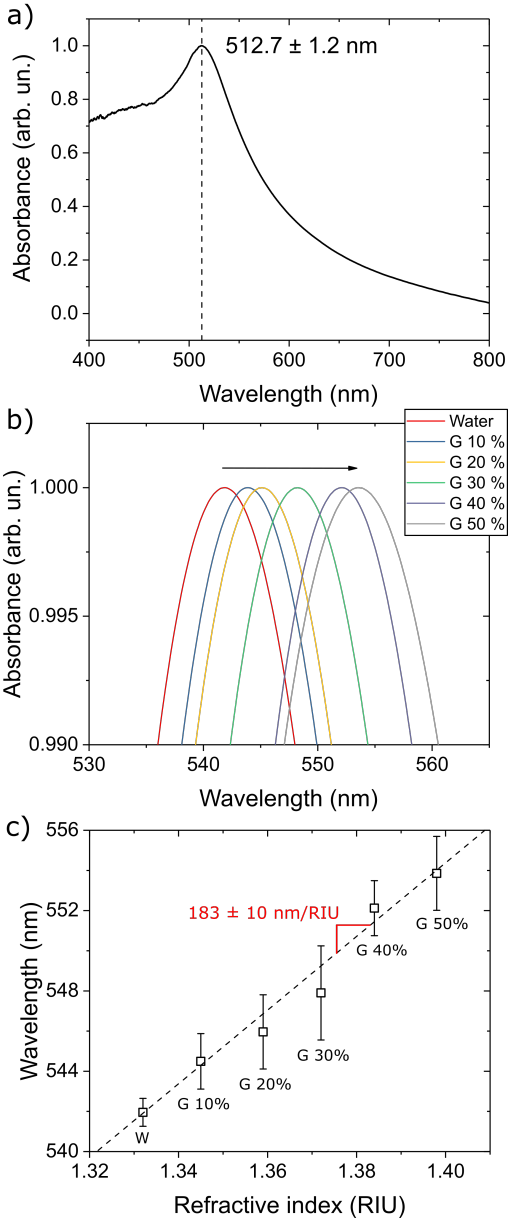

Figure 3: (a) Normalized average absorbance spectrum for gold spikes fabricated with 480 s ED time. The plot is the average of 25 spectra collected on different substrate positions on different samples. (b) Absorption spectra resulting from the exposure of gold nanospikes to aqueous solutions with different refractive indices: water (W) and water/glycerol (G) mixtures with varying concentrations 10 to 50% w/w. The black arrow highlights the red shift in the resonance peak due to the increase in the refractive index of the solution. (c) The refractive index sensitivity of the gold nanospike substrate is calculated by linear regression from LSPR peak shifts recorded for water and glycerol mixtures shown in (b).

We further verify the sensor selectivity by measuring its response against three different analytes (i.e., 100 μg/mL BSA, 10 μg/mL IL-6, 1 μg/mL CRP, and a mixture of these three analytes at 1 μg/mL). In principle, if our sensor platform is selective, these analytes should not bind with the immobilized murine IgG, hence no signal response should be detected within the instrument error range. As shown in Fig. 4c, the three analytes and their mixture at various concentrations produce minimal blue shifts in the average LSPR peak position, which is reasonable considering the

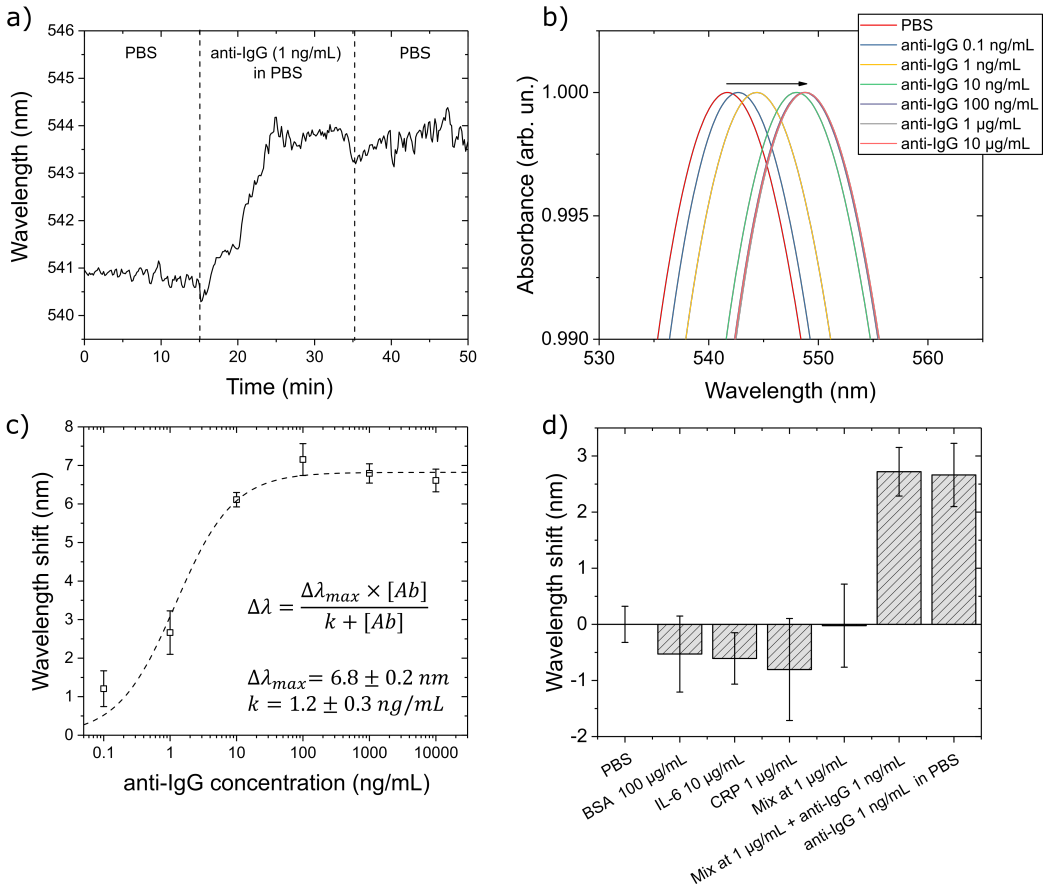

Figure 4: LSPR response for an IgG/anti-IgG model system in the opto-microfluidic platform. (a) Typical sensorgram corresponding to the detection of 1 ng/mL of IgG antibody in PBS. The vertical dashed lines highlight each step of the protocol described in the text. (b) Absorption spectra of the functionalized gold nanospikes upon exposure to IgG antibody at varying concentrations. The antigen-antibody binding occurring on the surface of the Au nanospikes increases the local RI, causing the red shift of the LSPR peak position (see the black arrow). (c) LSPR response at different IgG antibody concentrations. Each data point corresponds to averaged data from triplicate experiments, with the error bars denoting the standard deviation. (d) Specificity test against BSA (100 μg/mL), IL-6 (10 μg/mL), CRP (1 μg/mL) and a mixture of these analytes at 1 μg/mL. All these samples produce negligible wavelength shifts falling under the experimental error. However, when 1 ng/mL of anti-IgG is added to the mixture, the wavelength shift is similar to that measured in the PBS with 1 ng/mL of anti-IgG.

relatively high analyte concentration used for the specificity measurements (i.e., 1 to 100 μg/mL, much higher than the concentration range showing the linear response with our opto-microfluidic sensor platform). Nevertheless, these small blue wavelength shifts are still comparable with the baseline (i.e., PBS) signals. Finally, we measure the LSPR peak shift of the mixture of BSA, IL-6 and CRP at 1 μg/mL enriched with 1 ng/mL of anti-IgG. The LSPR wavelength shift is very similar to the value obtained in the PBS with 1 ng/mL of anti-IgG. This implies that the signals captured in our opto-microfluidic chip are not affected by the presence of interfering molecules such as BSA, CRP, and IL-6, but corresponding to the true antigen-antibody interactions.

3.3. Anti-SARS-CoV-2 Spike Protein Antibody Detection in PBS

The sensing procedure optimized for the IgG/anti-IgG model system is next applied to detect antibodies against the SARS-CoV-2 spike protein. In this case, the immobilized antigen is a peptide from the spike protein, which can be easily replaced with the whole protein or with different viral antigens if necessary. Similarly, the surface functionalization steps are first verified by measuring the LSPR peak shift in air (Fig. S5b). While the immobilization

of the murine IgG in the previous experiments produced a wavelength shift of ≈ 5 nm (Fig. S5a), the immobilization of the SARS-CoV-2 Spike protein peptide exhibits a 3.5 nm of shift (Fig. S5b). This is reasonable considering the smaller size of the spike protein fragment (20 amino acids; ≈ 2 kDa) in comparison to the size of a whole IgG (≈ 150 kDa).

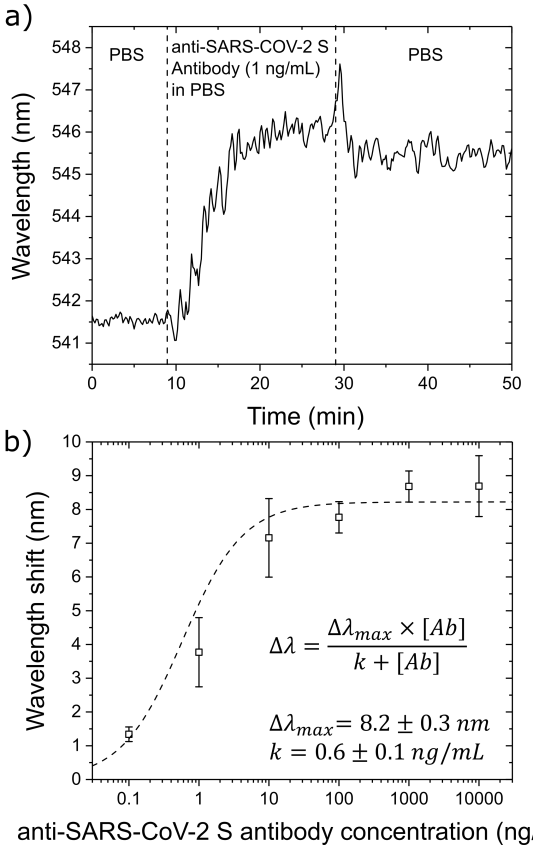

Figure 5: LSPR response in detecting antibodies against the SARS-CoV-2 Spike protein in the opto-microfluidic platform. (a) Typical sensorgram corresponding to the detection of 1 ng/mL of anti-SARS-CoV-2 Spike protein antibody in PBS. The vertical dashed lines highlight the initial wavelength stabilization in PBS, the injection of the antibody sample, and the final washing step with PBS to remove weakly bonded molecules. (b) LSPR responses at different anti-SARS-CoV-2 spike protein antibody concentrations. Each data point corresponds to the average data from triplicate experiments, with the error bars denoting the standard deviation.

The sensorgram displays the detection of 1 ng/mL of anti-SARS-CoV-2 spike protein antibody in PBS in Fig. 5a. Comparing this output with the analogous experiment performed on IgG/anti-IgG (Fig. 4a), the antibody against the spike protein produces a larger wavelength shift (≈ 4 nm) at 1 ng/mL, which suggests a higher affinity between the spike peptide and its antibody. This is supported by the complete calibration of the sensor response shown in Fig. 5b.

The best fit of the LSPR responses at different antibody concentrations gives the values of $\Delta\lambda_{max} = 8.2 \pm 0.3$ nm and $k = 0.6 \pm 0.1$ ng/mL by using Eq. 1. The higher affinity of the anti-SARS-CoV-2 spike protein antibody for the immobilized antigen (i.e., lower k value) implies higher detection sensitivity and results in a steeper response in the calibration plot. On the other hand, the larger saturation value (8.2 ± 0.3 nm versus 6.8 ± 0.2 nm for IgG/anti-IgG) can be explained considering the different sizes of the immobilized antigens (i.e., a fragment of the SARS-CoV-2 Spike protein and a whole IgG). The LOD related to the SARS-CoV-2 spike protein is ≈ 0.08 ng/mL (≈ 0.5 pM), which falls under the clinical relevant concentration range, since the concentration of specific antibodies produced in response to an infection are usually ≈ mg/mL in the serum of convalescent patients (Brown et al., 2018; Humphrey and Batty, 1974; Long et al., 2020; Okba et al., 2020). Note that the LOD (≈ 0.5 pM) obtained by our opto-microfluidic platform is comparable or better than existing optical biosensors used to detect antibodies (Xu et al., 2020), usually in the pM–nM

concentration range (Vaisocherová et al., 2007; Della Ventura et al., 2019; Kausaite-Minkstimiene et al., 2009).

3.4. Anti-SARS-CoV-2 spike Protein Antibody Detection in Human Plasma

We first check whether our sensing procedure is effected by the plasma components (e.g., fibrinogen, albumin, globulins, etc.) present in a diluted blood plasma solution (1:1000 in PBS, with 1 μL of human plasma). The sensor response of the dilute blood plasma (red curve in Fig. 6a) is very similar to that of a pure PBS solution, indicating that within the experimental error, the plasma components do not interfere with the quantification of the target antibody. However, the diluted human plasma does require slightly longer time ($\approx$ 20 min) to stabilize the sensor signal (i.e., wavelength shift) due to the presence of the plasma components. We then validate our opto-microfluidic platform to detect SARS-CoV-2 spike protein by using the diluted blood plasma enriched with anti-SARS-CoV-2 spike protein antibodies at concentrations of 1, 10 and 100 ng/mL. The black curve in Fig. 6a is the sensorgram corresponding to the detection of 1 ng/mL of anti-SARS-CoV-2 spike protein antibody in diluted human plasma.

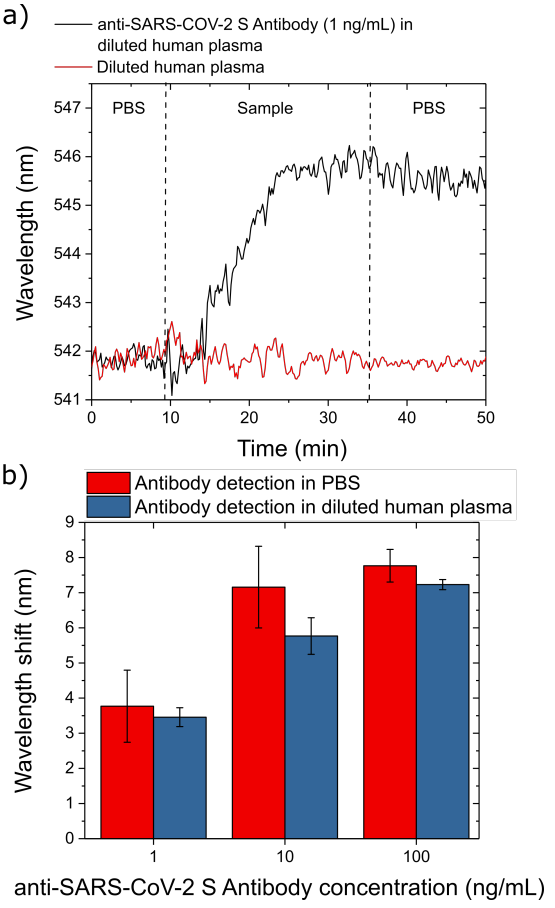

Figure 6: LSPR response in detecting antibodies against the SARS-CoV-2 spike protein in a diluted human plasma. (a) Typical sensorgrams corresponding to the detection of 1 ng/mL of anti-SARS-CoV-2 spike protein antibodies in diluted human plasma (black line) and sensor response against diluted human plasma without the target antibody (red line). The vertical dashed lines highlight each step of the protocol described in the text. (b) LSPR response at different anti-SARS-CoV-2 Spike protein antibody concentrations in PBS (red bars) and diluted plasma (blue bars). Each data point corresponds to the average value measured in 3 experiments, with the error bars denoting the standard deviation.

For all 3 concentrations of anti-SARS-CoV-2 spike protein antibodies tested (Fig. 6), the LSPR responses in diluted plasma (blue bars) are on average slightly smaller than those measured in the PBS (red bars). These small differences are possibly caused by the presence of various proteins and molecules in the human plasma sample and are negligible since they fall within the experimental error. The anti-SARS-CoV-2 Spike protein antibody concentrations tested in this experiment cover the clinical relevant range for specific antibodies in plasma, and can be further extended to lower

concentrations considering the high sensitivity of our opto-microfluidic platform (i.e., LOD $\approx$ 0.08 ng/mL).

Recall that rapid diagnostic tests (usually 10–30 min) such as lateral flow assays use blood from a finger prick, saliva samples, or nasal swab fluids to check the presence of the antibodies against a specific target (i.e., the SARS-CoV-2 antigens in this case). However, these tests tend to have lower accuracy and provide only qualitative (i.e., positive or negative) information about the antibody concentration in the patient's sample, hence their usage is limited to preliminary and fast point-of-care tests. On the other hand, lab-based tests provide quantification of the amount of antibodies in patients' samples such as blood. For instance, neutralization assay relies on the capability of the patient's antibodies to neutralize the virus and protect cells from the infection. This technique requires whole blood, serum, or plasma samples and takes 3–5 days to complete the analysis. Chemiluminescent immunoassays also use whole blood, plasma, or serum samples to quantify the number and isotype of the antibodies. The sample is mixed with a reaction solution and the antibodies are quantified by measuring the emitted light resulting from an enzymatic reaction. The total assay time takes approximately 2 h. ELISA-based techniques rely on the incubation of the biological fluid with a plate coated with viral antigens (i.e., SARS-CoV-2 spike protein), and the amount of bonded antibodies is quantified by a colorimetric or fluorescent-based signal. The whole assay procedure usually requires 2–5 hours. All these techniques provide quantitative and reliable analysis, but they require experienced operators, bulky and expensive laboratory equipment, and usually take at least hours of assay time to obtain the results.

We compare our opto-microfluidic sensing platform with the existing commercial serological assays reported by the most up-to-date survey (approved for EUA by FDA), focusing on the performance parameters such as the assay principle, target molecules, portability, assay time, user experience requirement, and susceptibility to false negative results (see details in Table S1 in the Supplementary Materials). Our opto-microfluidic sensing platform combines the fast quantitative detection of antibodies in plasma, which is achieved in $\approx$ 30 min with a small sample volume (i.e., only 1 μL of plasma is required), with an easy-to-use and compact device, therefore is also suitable for point-of-care tests. The LOD of our platform (0.5 pM) is comparable with those offered by laboratory methodologies, including commercial ELISA kits, that usually fall in the pM concentration range (Zhang et al., 2014). For example, the LOD obtained using our platform against 1:1000 diluted spiked human plasma sample is 0.08 ng/mL, while the LOD from commercial ELISA assays ranges 1.6–13500 ng/mL by using real patient samples. More details can be found in Table S1 in the Supplementary Material. We would like to emphasize that ELISA assays rely on signal amplifications based on horseradish peroxidase or fluorescence to enhance the detection sensitivity, while our LSPR based opto-microfluidic platform is label free, which can significantly reduce the assay time and the amount of chemical consumption, and consequently the overall assay costs. However, our current platform is still at proof-of-concept stage and our results are based on artificial human plasma samples doped with anti-SARS-CoV-19 S antibodies produced in rabbit. Our future work aims to collaborate with local hospitals to perform assays with real covid-19 patient samples to validate and compare the true performance with the existing serological antibody assays.

4. Conclusions

In this work, we report the development and the detailed characterization of an opto-microfluidic sensing platform based on Au nanospikes fabricated by electrodeposition for the detection of anti-SARS-CoV-2 spike protein antibodies. This is performed in diluted human plasma without any labelling agents, reaching a LOD of $\approx$ 0.08 ng/mL ($\approx$ 0.5 pM), which falls under the clinical relevant concentration range of specific antibodies against bacteria or viruses responsible for the infection. Our sensing platform shows great potential to complement the existing serological COVID-19 antibody tests. Since the nanofabrication process involved to assemble the sensing platform is simple, fast and cheap, the mass production of our opto-microfluidic platforms is feasible. The integration of fiber optics in a microfluidic device makes the entire platform very compact and easy to operate even for inexperienced users. Our device is suitable to analyze diluted blood plasma, which is a common practice in serological assays. We intend to collaborate with local hospitals and medical institutions to perform tests on real patient samples. This will be critical to validate our sensing platform for antibody tests for COVID-19 pandemic. To improve the performance of our opto-microfluidic platform, we also plan to optimize the electrodeposition procedure to fabricate gold nanostructures with smaller spacing and higher aspect ratio, so that the antibody-antigen binding can produce a larger shift in the LSPR peak and, consequently, increase the signal-to-noise ratio of the sensor. Finally, we aim to expand our current platform for multiplexing, which is crucial to make diagnosis more accurate by detecting multiple biomarkers, such as antibodies against other COVID-19 structural proteins (membrane, the envelope, and the nucleocapsid proteins).

CRediT authorship contribution statement

Riccardo Funari: Conceptua0lization of this study, Methodology, Funding acquisition, Data analysis, Writing the manuscript. **Kang-Yu Chu:** Methodology, Software Development. **Amy Q Shen:** Conceptualization of this study, Funding acquisition, Supervision, Writing the manuscript.

Acknowledgements

The authors thank Dr. Alessandro Giussani from Mathematics, Mechanics, and Materials Unit at OIST for the XRD analysis of the gold nanospikes, Ms. Shivani Sathish and Dr. Hsieh-Fu Tsai from Micro/Bio/Nanofluidics Unit at OIST for their constructive feedback on the manuscript. The authors acknowledge the support of the Okinawa Institute of Science and Technology Graduate University with subsidy funding from the Cabinet Office, Government of Japan. R.F. acknowledges funding from the Japanese Society for the Promotion of Science (Grants-in-Aid for Early-Career Scientists, Grant # 20K20237). A.Q.S. acknowledges funding from the Japanese Society for the Promotion of Science (Grants-in-Aid for Scientific Research (B), Grant # 18H01135).

References

F. Wu, S. Zhao, B. Yu, Y.-M. Chen, W. Wang, Z.-G. Song, Y. Hu, Z.-W. Tao, J.-H. Tian, Y.-Y. Pei, et al., Nature **579**, 265 (2020).
A. S. Fauci, H. C. Lane, and R. R. Redfield, The New England Journal of Medicine **382**, 1268 (2020).
R. Li, S. Pei, B. Chen, Y. Song, T. Zhang, W. Yang, and J. Shaman, Science **368**, 489 (2020).
S. Zhao, S. S. Musa, Q. Lin, J. Ran, G. Yang, W. Wang, Y. Lou, L. Yang, D. Gao, D. He, et al., Journal of Clinical Medicine **9**, 388 (2020).
C. Dincer, R. Bruch, E. Costa-Rama, M. T. Fernández-Abedul, A. Merkoçi, A. Manz, G. A. Urban, and F. Güder, Advanced Materials **31**, 1806739 (2019).
J. R. Choi, Frontiers in Chemistry **8**, 517 (2020).
E. Morales-Narváez and C. Dincer, Biosensors and Bioelectronics **163**, 112274 (2020).
H. Zhu, Z. Fohlerová, J. Pekárek, E. Basova, and P. Neužil, Biosensors and Bioelectronics **153**, 112041 (2020).
I. Santiago, ChemBioChem **21**, 1 (2020).
G. Seo, G. Lee, M. J. Kim, S.-H. Baek, M. Choi, K. B. Ku, C.-S. Lee, S. Jun, D. Park, H. G. Kim, et al., ACS Nano **14**, 5135 (2020).
N. Bhalla, Y. Pan, Z. Yang, and A. F. Payam, ACS Nano **in press** (2020).
V. M. Corman, O. Landt, M. Kaiser, R. Molenkamp, A. Meijer, D. K. Chu, T. Bleicker, S. Brünink, J. Schneider, M. L. Schmidt, et al., Eurosurveillance **25**, 2000045 (2020).
D. K. Chu, Y. Pan, S. M. Cheng, K. P. Hui, P. Krishnan, Y. Liu, D. Y. Ng, C. K. Wan, P. Yang, Q. Wang, et al., Clinical Chemistry **66**, 549 (2020).
P. Moitra, M. Alafeef, K. Dighe, M. Frieman, and D. Pan, ACS Nano **14**, 7617 (2020).
A. La Marca, M. Capuzzo, T. Paglia, L. Roli, T. Trenti, and S. M. Nelson, Reproductive BioMedicine Online **in press** (2020).
K. J. Paiva, R. D. Grisson, P. A. Chan, J. R. Lonks, E. King, R. C. Huard, D. L. Pytel-Parenteau, G. H. Nam, E. Yakirevich, and S. Lu, bioRxiv (2020).
Z. Du, F. Zhu, F. Guo, B. Yang, and T. Wang, Journal of Medical Virology **in press** (2020).
F. Cui and H. S. Zhou, Biosensors and Bioelectronics **165**, 112349 (2020).
M. Day, BMJ: British Medical Journal (Online) **368** (2020).
F. Krammer and V. Simon, Science **368**, 1060 (2020).
A. K. Winter and S. T. Hegde, The Lancet Infectious Diseases **20**, 758 (2020).
Q.-X. Long, B.-Z. Liu, H.-J. Deng, G.-C. Wu, K. Deng, Y.-K. Chen, P. Liao, J.-F. Qiu, Y. Lin, X.-F. Cai, et al., Nature Medicine (2020).
J. D. Roback and J. Guarner, JAMA **323**, 1561 (2020).
K. Duan, B. Liu, C. Li, H. Zhang, T. Yu, J. Qu, M. Zhou, L. Chen, S. Meng, Y. Hu, et al., Proceedings of the National Academy of Sciences **117**, 9490 (2020).
F. Amanat, D. Stadlbauer, S. Strohmeier, T. H. Nguyen, V. Chromikova, M. McMahon, K. Jiang, G. A. Arunkumar, D. Jurczyszak, J. Polanco, et al., Nature Medicine **26**, 1033âĂŞ1036 (2020).
C. Y.-P. Lee, R. T. Lin, L. Renia, and L. F. Ng, Frontiers in Immunology **11**, 879 (2020).
U.S. Food and Drug Administration, *EUA Authorized Serology Test Performance* (2020), accessed: 2020-08-15, URL https://www.fda.gov/medical-devices/emergency-situations-medical-devices/eua-authorized-serology-test-performance.
A. E. Muruato, C. R. Fontes-Garfias, P. Ren, M. A. Garcia-Blanco, V. D. Menachery, X. Xie, and P.-Y. Shi, bioRxiv (2020).
John Hopkins Center for Health Security, *Global progresses on serology-based tests for covid-19* (2020), accessed: 2020-08-15, URL https://www.centerforhealthsecurity.org/resources/COVID-19/serology/Serology-based-tests-for-COVID-19.html.
L. J. Carter, L. V. Garner, J. W. Smoot, Y. Li, Q. Zhou, C. J. Saveson, J. M. Sasso, A. C. Gregg, D. J. Soares, T. R. Beskid, et al., ACS Central Science **6**, 591 (2020).
B. Udugama, P. Kadhiresan, H. N. Kozlowski, A. Malekjahani, M. Osborne, V. Y. Li, H. Chen, S. Mubareka, J. B. Gubbay, and W. C. Chan, ACS Nano **14**, 3822 (2020).
W. Xu, D. Wang, D. Li, and C. C. Liu, International Journal of Molecular Sciences **21**, 134 (2020).
Z. Huang, D. Tian, Y. Liu, Z. Lin, C. Lyon, W. Lai, D. Fusco, A. Drouin, X. Yin, T. Hu, et al., Biosensors and Bioelectronics **164**, 112316 (2020).
G. Qiu, Z. Gai, Y. Tao, J. Schmitt, G. A. Kullak-Ublick, and J. Wang, ACS Nano **14**, 5268 (2020).

S. Mavrikou, G. Moschopoulou, V. Tsekouras, and S. Kintzios, Sensors **20**, 3121 (2020).
A. Ahmadivand, B. Gerislioglu, Z. Ramezani, A. Kaushik, P. Manickam, and S. A. Ghoreishi, arXiv (2020), 2006.08536.
L. Zeng, Y. Li, L. Guo, Z. Wang, X. Xu, S. Song, C. Hao, L. Liu, M. Xin, and C. Xu, Materials Chemistry Frontiers **4**, 2000 (2020).
K. A. Willets and R. P. Van Duyne, Annu. Rev. Phys. Chem. **58**, 267 (2007).
K. M. Mayer and J. H. Hafner, Chemical Reviews **111**, 3828 (2011).
S. Szunerits and R. Boukherroub, Chemical Communications **48**, 8999 (2012).
J. F. Brown, J. M. Dye, S. Tozay, G. Jeh-Mulbah, D. A. Wohl, W. A. Fischer 2nd, C. K. Cunningham, K. Rowe, P. Zacharias, J. van Hasselt, et al., The Journal of Infectious Diseases **218**, 555 (2018).
J. Humphrey and I. Batty, Clinical and Experimental Immunology **17**, 708 (1974).
Y. M. Sabri, S. J. Ippolito, J. Tardio, V. Bansal, A. P. O'Mullane, and S. K. Bhargava, Scientific Reports **4**, 1 (2014).
Y. Tian, H. Liu, G. Zhao, and T. Tatsuma, The Journal of Physical Chemistry B **110**, 23478 (2006).
S. Cherevko and C.-H. Chung, Electrochemistry Communications **13**, 16 (2011).
Y. M. Sabri, A. E. Kandjani, S. J. Ippolito, and S. K. Bhargava, Scientific Reports **6**, 1 (2016).
N. S. Lopa, M. M. Rahman, F. Ahmed, T. Ryu, S. C. Sutradhar, J. Lei, J. Kim, D. H. Kim, Y. H. Lee, and W. Kim, Biosensors and Bioelectronics **126**, 381 (2019).
M. Mohammadniaei, A. Go, S. G. Chavan, A. Koyappayil, S.-E. Kim, H. J. Yoo, J. Min, and M.-H. Lee, Biosensors and Bioelectronics **141**, 111468 (2019).
K. J. Stine, Applied Sciences **9**, 797 (2019).
H. Chen, X. Kou, Z. Yang, W. Ni, and J. Wang, Langmuir **24**, 5233 (2008).
B. Kurganov, A. Lobanov, I. Borisov, and A. Reshetilov, Analytica Chimica Acta **427**, 11 (2001).
J. N. Weiss, The FASEB Journal **11**, 835 (1997).
G. L. Long and J. D. Winefordner, Analytical Chemistry **55**, 712A (1983).
N. M. Okba, M. A. Müller, W. Li, C. Wang, C. H. GeurtsvanKessel, V. M. Corman, M. M. Lamers, R. S. Sikkema, E. de Bruin, F. D. Chandler, et al., Emerging Infectious Diseases **26** (2020).
H. Vaisocherová, K. Mrkvová, M. Piliarik, P. Jinoch, M. Šteinbachová, and J. Homola, Biosensors and Bioelectronics **22**, 1020 (2007).
B. Della Ventura, M. Gelzo, E. Battista, A. Alabastri, A. Schirato, G. Castaldo, G. Corso, F. Gentile, and R. Velotta, ACS Applied Materials & Interfaces **11**, 3753 (2019).
A. Kausaite-Minkstimiene, A. Ramanaviciene, and A. Ramanavicius, Analyst **134**, 2051 (2009).
S. Zhang, A. Garcia-D'Angeli, J. P. Brennan, and Q. Huo, Analyst **139**, 439 (2014).